Multiphysics Modeling of Plasmonic Organic Solar Cells with a Unified Finite-Difference Method

Wei E.I. Sha and Wallace C.H. Choy
Department of Electrical and Electronic Engineering
the University of Hong Kong
Pokfulam Road, Hong Kong
Emails: wsha@eee.hku.hk; chchoy@eee.hku.hk

Weng Cho Chew
Department of Electrical and Computer Engineering
University of Illinois
Urbana-Champaign, Illinois 61801, USA
Email: w-chew@uiuc.edu

***Abstract*—A multiphysics study carries out on plasmonic organic solar cells (OSCs) by solving Maxwell's equations and semiconductor (Poisson, drift-diffusion, and continuity) equations simultaneously with unified finite-difference framework. Regarding the Maxwell's equations, the perfectly matched layer and periodic boundary conditions are imposed at the vertical and lateral directions of OSCs to simulate the infinite air region and metallic grating electrode, respectively. In view of the semiconductor equations, the Scharfetter-Gummel scheme and semi-implicit strategy are adopted respectively in the space and time domains. To model the bulk heterojunction OSCs, the Langevin bimolecular recombination and Onsager-Braun exciton dissociation models are fully taken into account. The exciton generation rate depending on the optical absorption of the organic active material can be obtained by solving the Maxwell's equations and will be inserted into the semiconductor equations. Through the multiphysics model, we observed the increased short-circuit current and dropped fill factor when OSCs incorporate a metallic grating anode supporting surface plasmon resonances. This work provides fundamental multiphysics modeling and understanding for plasmonic organic photovoltaics.**

I. Introduction

As one of the promising candidates for photovoltaic applications, organic solar cells (OSCs) have drawn considerable attention recently due to their properties of large-area production, mechanical flexibility, and low-cost processing [1], [2]. However, the short lifetime and diffusion length of excitons result in ultrathin active-layer configuration in OSCs. The configuration limits the light absorption efficiency, and thereby the power conversion efficiency. The power conversion efficiency (PCE) of OSCs is given by PCE $= J_{sc}V_{oc}\text{FF}/P_{in}$, where J_{sc} is the short-circuit current, V_{oc} is the open-circuit voltage, FF is the fill factor (FF), and P_{in} is the incident photon power. Having unique features of tunable resonance and unprecedented near-field concentration, plasmonics is one of enabling techniques for boosting the optical absorption of OSCs [3], [4], [5], [6]. The enhanced optical absorption substantially increases the generation rate of photocarriers and thus short-circuit current. The basic device physics of OSCs has been investigated in literatures [7], [8]. However, the physical mechanism of the modified electrical properties of OSCs due to the introduction of metallic nanostructures has not been unveiled systematically. Apart from the optical absorption properties [3], [4], [5], [6], the electrical properties of plasmonic OSCs, such as internal E-field distribution, recombination loss, and exciton dissociation, will greatly affect the performance of organic solar cell (OSC) devices.

In this paper, we model the optical and electrical properties of OSCs with the metallic grating and planar anodes through solving Maxwell's equations and semiconductor equations simultaneously. The photocarrier's generation, transport, and collections are fully observed and comparatively studied for plasmonic OSCs with the gating anode and standard OSCs with the planar anode. The multiphysics modeling and understanding are imperative for high-efficiency organic photovoltaic technique and low-cost green energy industry.

II. Unified Finite-Difference Method

A. Maxwell's equations

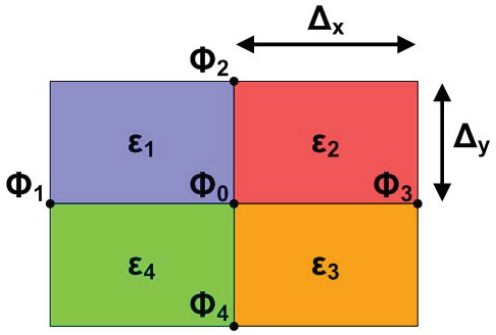

Fig. 1. (Color online) The five-point stencil for the FDFD method. Δ_x and Δ_y are respectively the spatial steps along the x and y directions. $\Phi = E_z$ for the TE polarization and $\Phi = H_z$ for the TM polarization. Here, $\epsilon = n_c^2$ is the relative permittivity in the discretized region and n_c is the complex refractive index of the optical material.

Considering a two-dimensional OSC structure, the Maxwell's equations can be decoupled into a TE and TM modes. The wave equations for TE and TM modes are respectively formulated as

$$\frac{1}{\epsilon_r}\frac{\partial}{\partial x}\left(\frac{1}{\mu_r}\frac{\partial E_z}{\partial x}\right)+\frac{1}{\epsilon_r}\frac{\partial}{\partial y}\left(\frac{1}{\mu_r}\frac{\partial E_z}{\partial y}\right)+k_0^2E_z=0 \quad (1)$$

$$\frac{1}{\mu_r}\frac{\partial}{\partial x}\left(\frac{1}{\epsilon_r}\frac{\partial H_z}{\partial x}\right)+\frac{1}{\mu_r}\frac{\partial}{\partial y}\left(\frac{1}{\epsilon_r}\frac{\partial H_z}{\partial y}\right)+k_0^2H_z=0 \quad (2)$$

where k_0 is the wave number of incident light, and ϵ_r and μ_r are the relative permittivities and permeabilities, respectively.

978-1-4799-0359-7/13/$31.00 ©2013 IEEE

Regarding non-magnetic optical materials, $\mu_r = 1$, $\epsilon_r = n_c^2$, and n_c is the complex refractive index of optical materials.

With the Yee lattice, the 2D finite-difference frequency-domain (FDFD) method [9] is utilized to characterize the optical properties of OSCs. As shown in Fig. 1, the five-point stencil is adopted for the FDFD method. The discretized forms for the TE (E_z) and TM (H_z) wave equations are respectively of the form

$$2\left(\frac{1}{\Delta_x^2}+\frac{1}{\Delta_y^2}\right)\frac{\Phi_0}{\bar{\epsilon}}-k_0^2\Phi_0-\frac{\Phi_1+\Phi_3}{\bar{\epsilon}\Delta_x^2}-\frac{\Phi_2+\Phi_4}{\bar{\epsilon}\Delta_y^2}=0 \tag{3}$$

$$\begin{aligned}2\left(\frac{1}{\Delta_x^2}+\frac{1}{\Delta_y^2}\right)\frac{\Phi_0}{\bar{\epsilon}}-k_0^2\Phi_0-\frac{\epsilon_1^{-1}+\epsilon_4^{-1}}{2\Delta_x^2}\Phi_1-\frac{\epsilon_2^{-1}+\epsilon_3^{-1}}{2\Delta_x^2}\Phi_3\\ -\frac{\epsilon_1^{-1}+\epsilon_2^{-1}}{2\Delta_y^2}\Phi_2-\frac{\epsilon_3^{-1}+\epsilon_4^{-1}}{2\Delta_y^2}\Phi_4=0\end{aligned} \tag{4}$$

$$\bar{\epsilon}=\begin{cases}\dfrac{\epsilon_1+\epsilon_2+\epsilon_3+\epsilon_4}{4}, & \Phi=E_z\\ 4(\epsilon_1^{-1}+\epsilon_2^{-1}+\epsilon_3^{-1}+\epsilon_4^{-1})^{-1}, & \Phi=H_z\end{cases} \tag{5}$$

The incident Sunlight reflected by OSC devices converts to outgoing waves propagating into infinite air (or free-space) region. A perfectly matched layer (PML) absorbs the outgoing waves without spurious reflections and "perfectly" simulates unbounded wave propagations. The wave equation with the complex coordinate stretched PML is given by

$$\frac{1}{s_r(x)}\frac{\partial}{\partial x}\left(\frac{1}{s_r(x)}\frac{\partial\Phi}{\partial x}\right)+\frac{1}{s_r(y)}\frac{\partial}{\partial y}\left(\frac{1}{s_r(y)}\frac{\partial\Phi}{\partial y}\right)+k_0^2\Phi=0 \tag{6}$$

where $s_r = 1 + i_0\sigma/\omega\epsilon_0$, i_0 is the imaginary unit, ϵ_0 is the permittivity of free-space, and the conductivities $\sigma(x)$ and $\sigma(y)$ are non-zeros only within PML layers normal to the x- and y-axes, respectively. The optimized conductivities are chosen as,

$$\begin{aligned}\sigma_i&=\frac{0.02}{\Delta}\left(\frac{2i-1}{16}\right)^{3.7}, \quad i=1,...,8\\ \sigma_{i+0.5}&=\frac{0.02}{\Delta}\left(\frac{2i}{16}\right)^{3.7}, \quad i=0,...,8\end{aligned} \tag{7}$$

where $\Delta = \Delta_x$ or $\Delta = \Delta_y$ for the PML layers normal to the x- or y-axis, and i is the grid index of the eight-layer PML.

Regarding a periodic OSC device, the periodic boundary conditions need to be implemented. According to the Floquet or Bloch theorem, we have

$$\begin{aligned}\Phi(x+P,y)&=\Phi(x,y)\exp\left(i_0k_0\sin\theta\cdot P\right)\\ \Phi(x,y)&=\Phi(x+P,y)\exp\left(-i_0k_0\sin\theta\cdot P\right)\end{aligned} \tag{8}$$

where P is the periodicity and θ is the incident angle with respect to the y axis.

B. Extraction of exciton generation rate

The exciton generation rate can be written as

$$G(\mathbf{r})=\int_{400\,\mathrm{nm}}^{800\,\mathrm{nm}}\frac{2\pi}{h}n_r(\lambda)k_i(\lambda)\epsilon_0|\mathbf{E}(\mathbf{r},\lambda)|^2\Gamma(\lambda)d\lambda \tag{9}$$

where h is the Planck constant, $n_c = n_r + i_0k_i$ is the complex refractive index of the active polymer material, $\mathbf{E}$ is the (optical) electric field that can be obtained by solving the Maxwell's equations, and Γ is the solar irradiance spectrum of AM 1.5G. Moreover, the exciton generation rate is the average value of those for TE and TM polarizations.

C. Semiconductor equations

For studying electrical properties of OSCs, one should self-consistently solve the coupled nonlinear semiconductor equations (Poisson, continuity, and drift-diffusion equations) given by

$$\nabla\cdot(\epsilon^d\nabla\phi)=-q(p-n) \tag{10}$$

$$\frac{\partial n}{\partial t}=\frac{1}{q}\nabla\cdot(-q\mu_n n\nabla\phi+qD_n\nabla n)+QG-(1-Q)R \tag{11}$$

$$\frac{\partial p}{\partial t}=\frac{-1}{q}\nabla\cdot(-q\mu_p p\nabla\phi-qD_p\nabla p)+QG-(1-Q)R \tag{12}$$

In the above, ϵ^d is the dielectric constant of the polymer active material, q is the electron charge, ϕ is the electrical potential, and n (p) is the electron (hole) concentration. Moreover, μ_n (μ_p) is the electron (hole) mobility, and D_n (D_p) is the electron (hole) diffusion coefficient accessible by Einstein relations and mobilities. Furthermore, $\mathbf{J}_n = -q\mu_n n\nabla\phi + qD_n\nabla n$ and $\mathbf{J}_p = -q\mu_p p\nabla\phi - qD_p\nabla p$ are respectively electron and hole current densities, and G is the exciton generation rate of Eq. (9) obtained with Maxwell's equations. In addition, R is the bimolecular recombination rate and Q is the field and temperature dependent exciton dissociation probability, which is a unique parameter for OSCs [10].

Using the Scharfetter-Gummel scheme in the spatial domain and using the semi-implicit strategy in the temporal domain [11], the 2D discretized forms of Eqs. (10) and (11) are respectively given by Eqs. (13) and (14), where $B(x) = \frac{x}{e^x-1}$ is the Bernoulli function and $U_t = \frac{k_BT}{q}$. It should be noted that the Gummel's method has been incorporated in (13) to accelerate the convergence of the nonlinear semiconductor equations.

The boundary conditions play a key role in modeling electrical properties of plasmonic OSCs. The potential boundary condition for the Schottky contact is given by

$$\phi=V_a-\frac{W_m}{q} \tag{15}$$

where V_a is the applied voltage, and W_m is the metal work function. For the ohmic contact, the built-in potential is the potential difference between the highest occupied molecular orbital (HOMO) of donor and lowest unoccupied molecular orbital (LUMO) of acceptor. The Neumann (floating) boundary condition is used to truncate the left and right boundaries of OSCs, i.e.

$$\frac{\partial\phi}{\partial N}=0,\ \frac{\partial n}{\partial N}=0,\ \frac{\partial p}{\partial N}=0 \tag{16}$$

$$\frac{1}{\Delta_x^2}\epsilon^d_{i+1/2,j}\phi^{t+1}_{i+1,j}+\frac{1}{\Delta_x^2}\epsilon^d_{i-1/2,j}\phi^{t+1}_{i-1,j}+\frac{1}{\Delta_y^2}\epsilon^d_{i,j+1/2}\phi^{t+1}_{i,j+1}+\frac{1}{\Delta_y^2}\epsilon^d_{i,j-1/2}\phi^{t+1}_{i,j-1}$$
$$-\left(\epsilon^d_{i+1/2,j}+\epsilon^d_{i-1/2,j}+\epsilon^d_{i,j+1/2}+\epsilon^d_{i,j-1/2}\right)\left(\frac{1}{2\Delta_x^2}+\frac{1}{2\Delta_y^2}\right)\phi^{t+1}_{i,j}-\frac{n^t_{i,j}+p^t_{i,j}}{U_t}\phi^{t+1}_{i,j} \tag{13}$$
$$=q(n^t_{i,j}-p^t_{i,j})-\frac{n^t_{i,j}+p^t_{i,j}}{U_t}\phi^t_{i,j}$$

$$\frac{n^{t+1}_{i,j}-n^t_{i,j}}{\Delta_t}=Q^t_{i,j}G_{i,j}-(1-Q^t_{i,j})R^t_{i,j}+\frac{D^n_{i+1/2,j}}{\Delta_x^2}B\left(\frac{\phi^{t+1}_{i+1,j}-\phi^{t+1}_{i,j}}{U_t}\right)n^{t+1}_{i+1,j}$$
$$+\frac{D^n_{i-1/2,j}}{\Delta_x^2}B\left(\frac{\phi^{t+1}_{i-1,j}-\phi^{t+1}_{i,j}}{U_t}\right)n^{t+1}_{i-1,j}+\frac{D^n_{i,j+1/2}}{\Delta_y^2}B\left(\frac{\phi^{t+1}_{i,j+1}-\phi^{t+1}_{i,j}}{U_t}\right)n^{t+1}_{i,j+1}$$
$$+\frac{D^n_{i,j-1/2}}{\Delta_y^2}B\left(\frac{\phi^{t+1}_{i,j-1}-\phi^{t+1}_{i,j}}{U_t}\right)n^{t+1}_{i,j-1}-\left[\frac{D^n_{i+1/2,j}}{\Delta_x^2}B\left(\frac{\phi^{t+1}_{i,j}-\phi^{t+1}_{i+1,j}}{U_t}\right)\right. \tag{14}$$
$$+\frac{D^n_{i-1/2,j}}{\Delta_x^2}B\left(\frac{\phi^{t+1}_{i,j}-\phi^{t+1}_{i-1,j}}{U_t}\right)+\frac{D^n_{i,j+1/2}}{\Delta_y^2}B\left(\frac{\phi^{t+1}_{i,j}-\phi^{t+1}_{i,j+1}}{U_t}\right)$$
$$\left.+\frac{D^n_{i,j-1/2}}{\Delta_y^2}B\left(\frac{\phi^{t+1}_{i,j}-\phi^{t+1}_{i,j-1}}{U_t}\right)\right]n^{t+1}_{i,j}$$

where N are the normal vectors of the left and right boundaries of OSCs. The boundary conditions for the top and bottom electrodes can be written as

$$n=N_c\exp\left(-\frac{\psi^n_b}{k_BT}\right),\ \text{for cathode} \tag{17}$$

$$p=N_v\exp\left(-\frac{\psi^p_b}{k_BT}\right),\ \text{for anode} \tag{18}$$

where N_c and N_v are the effective state density of electrons and holes, respectively. ψ^n_b is the injection barrier between the LUMO and the cathode, and ψ^p_b is the injection barrier between the HOMO and the anode. It should be noted that the infinite surface recombination velocity is assumed for the Schottky contact.

III. Results

The schematic standard and plasmonic OSC structures are shown in Figs. 2(a) and (b), respectively. The blend active layer of bulk heterojunction OSCs comprises a small bandgap donor of PBDTTT-C-T and an acceptor of $PC_{70}BM$. A silver rectangular-grating is introduced as the anode for the plasmonic OSC. Fig. 2(c) depicts the energy level diagram of the OSCs. The anode is assumed to be an ohmic contact while the cathode has an injection (Schottky) barrier of 0.2 eV. Figure 2(d) shows the ratio of the generation rate of the plasmonic OSC to that of the standard OSC. The extremely dense exciton generation can be found around the metallic grating. Moreover, the increased exciton generation can be observed in the active region below the ridge of the grating. From Fig. 2(d), the exciton generation is extremely nonuniform in the active layer of the plasmonic cell.

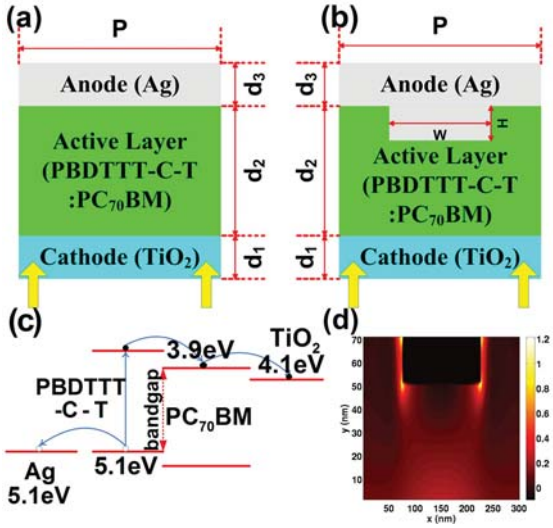

Fig. 2. (a,b) The schematic patterns for the unit cells of the standard and plasmonic OSCs, respectively. The geometric parameters are $d_1 = 30$ nm, $d_2 = 70$ nm, $d_3 = 30$ nm, $P = 300$ nm, $W = 150$ nm, and $H = 20$ nm. (c) The energy levels of active materials and electrodes. (d) The generation rate map of the plasmonic cell divided by that of the standard cell (in the active layer). The logarithmic scale is adopted.

Fig. 3 and Fig. 4 show the potential distribution, recombination rate, electron and hole current densities at the short-circuit condition for the standard and plasmonic OSCs, respectively. The plasmonic OSC has abnormal carrier transport and giant recombination loss compared to the standard one.

The short-circuit current of the plasmonic cell is improved by 13% due to the plasmon enhanced photoabsorption as depicted in Fig. 5. The slightly increased open-circuit voltage

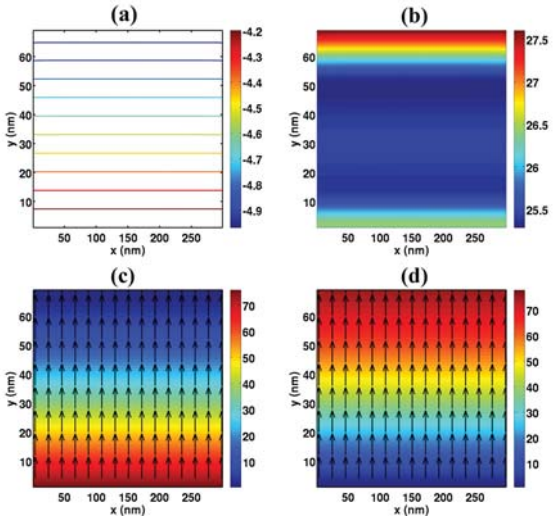

Fig. 3. The electrical results of the standard OSC at the short-circuit condition. (a) equipotential lines (V); (b) recombination rate with the logarithmic scale ($\mathrm{m^{-3}s^{-1}}$); (c,d) electron and hole current densities ($\mathrm{A/m^2}$). The color and arrow denote the amplitude and direction of the currents.

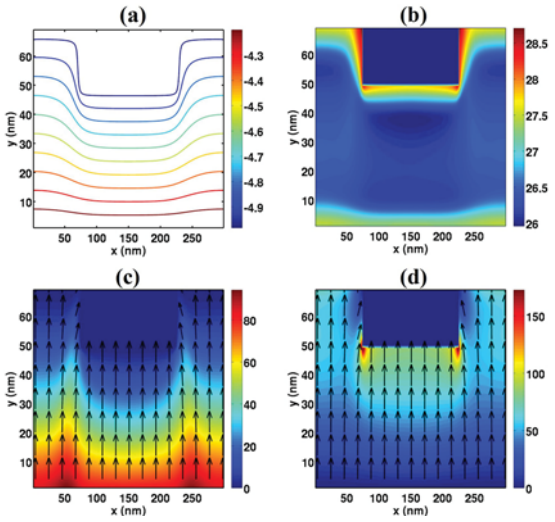

Fig. 4. The electrical results of the plasmonic OSC at the short-circuit condition. (a) equipotential lines (V); (b) recombination rate with the logarithmic scale ($\mathrm{m^{-3}s^{-1}}$); (c,d) electron and hole current densities ($\mathrm{A/m^2}$). The color and arrow denote the amplitude and direction of the currents.

in the plasmonic OSC may be attributed to the favorable hole transport. A lot of holes are generated around the grating anode and can be collected efficiently. The FF is defined by the maximum power output over the product of short-circuit current and open-circuit voltage. A significant 7% drop of the FF in the plasmonic cell is strongly confirmed by our multiphysics model. On one hand, the periodically-modulated metallic grating excites the concentrated plasmonic waves near the anode resulting in nonuniform photocarrier generation (Fig. 2(d)). On the other hand, the modulated anode boundary is responsible for inhomogeneous built-in potential and internal E-field distributions below ridge and troughs of the grating anode, which has strong effects on the photocarrier transport and collections.

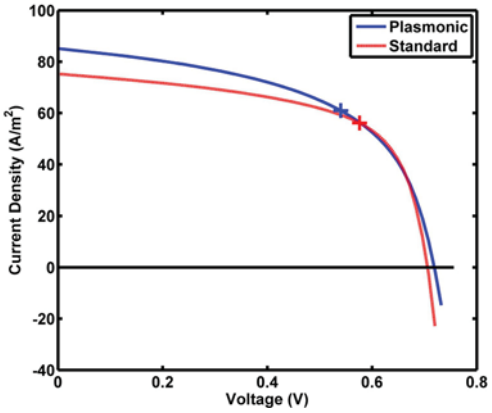

Fig. 5. The voltage-current density curve of the plasmonic and standard cells. The maximum power points are denoted by the plus signs.

IV. Conclusion

We have investigated the plasmonic OSC with the metallic rectangular-grating anode through the multiphysics solutions to Maxwell's equations and semiconductor equations with unified finite-difference method. The grating anode induces nonuniform optical absorption and inhomogeneous internal E-field distribution. Thus uneven photocarrier generation and transport are formed in the plasmonic OSC leading to the dropped FF. The multiphysics modeling and understanding are fundamentally important for improving the performance of organic photovoltaics.

References

[1] C. J. Brabec, S. Gowrisanker, J. J. M. Halls, D. Laird, S. J. Jia, and S. P. Williams, "Polymer-fullerene bulk-heterojunction solar cells," Adv. Mater. **22**, 3839–3856 (2010).

[2] C. Deibel and V. Dyakonov, "Polymer-fullerene bulk heterojunction solar cells," Rep. Prog. Phys. **73**, 096401 (2010).

[3] H. A. Atwater, and A. Polman, "Plasmonics for improved photovoltaic devices," Nat. Mater. **9**, 205 (2010).

[4] R. A. Pala, J. White, E. Barnard, J. Liu, and M. L. Brongersma, "Design of plasmonic thin-film solar cells with broadband absorption enhancements," Adv. Mater. **21**, 3504–3509 (2009).

[5] C. J. Min, J. Li, G. Veronis, J. Y. Lee, S. H. Fan, and P. Peumans, "Enhancement of optical absorption in thin-film organic solar cells through the excitation of plasmonic modes in metallic gratings," Appl. Phys. Lett. **96**, 133302 (2010).

[6] W. E. I. Sha, W. C. H. Choy, Y. G. Liu, and W. C. Chew, "Near-field multiple scattering effects of plasmonic nanospheres embedded into thin-film organic solar cells," Appl. Phys. Lett. **99**, 113304 (2011).

[7] L. J. A. Koster, E. C. P. Smits, V. D. Mihailetchi, and P. W. M. Blom, "Device model for the operation of polymer/fullerene bulk heterojunction solar cells," Phys. Rev. B **72**, 085205 (2005).

[8] V. D. Mihailetchi, J. Wildeman, and P. W. M. Blom, "Space-charge limited photocurrent," Phys. Rev. Lett. **94**, 126602 (2005).

[9] W. E. I. Sha, W. C. H. Choy, and W. C. Chew, "A comprehensive study for the plasmonic thin-film solar cell with periodic structure," Opt. Express **18**, 5993-6007 (2010).

[10] W. E. I. Sha, W. C. H. Choy, and W. C. Chew, "The roles of metallic rectangular-grating and planar anodes in the photocarrier generation and transport of organic solar cells," Appl. Phys. Lett. **101**, 223302 (2012).

[11] W. E. I. Sha, W. C. H. Choy, Y. Wu, and W. C. Chew, "Optical and electrical study of organic solar cells with a 2D grating anode," Opt. Express **20**, 2572-2580 (2012).